Structural and Multidisciplinary Optimization (2024) 67:204
https://doi.org/10.1007/s00158-024-03928-2

RESEARCH PAPER

Level-set-based topology optimization of threedimensional structures considering the manufacturing process with realistic milling tools

Christopher Colling[1,2] · Axel Schumacher[1] · Klaus Mecking[2]

Received: 29 November 2023 / Revised: 12 August 2024 / Accepted: 29 October 2024 / Published online: 27 November 2024

Abstract
In this work, we develop an approach for the level set based topology optimization of millable 3D structures. We focus on the 3-axis machining with realistic formed milling tools. The basis of the method lies in the identification of surface areas that cannot be reached by a given milling tool during optimization. For this purpose, we present an interpolation method that identifies these areas by an interpolation of the level set function along the outer contours of realistic milling tools, considering available machining directions. To minimize inaccessible surfaces, we define a potential field whose values decrease linearly into the outer normal direction of the structure. The inaccessible boundaries are pushed outward by minimizing their respective potential and therefore become accessible. Manufacturability is integrated into the optimization problem as an explicit constraint.

Keywords Topology optimization · Level set method · CNC milling · Manufacturing constraints · Subtractive manufacturing

1 Introduction

Algorithmic topology optimization has become an established part of the development processes for mechanical structures in recent decades. In particular, methods are used which divide the available design space into many small volumes and decide for each of these volumes whether there should be material there or not. This results in interpretable structures (Bendsøe and Sigmund 2004). These methods are also referred to as density methods. But also other approaches, such as CAD-based methods or the level-set method (Allaire et al 2004) can be used for topology optimization. Depending on the method used, relevant component properties can be considered in the optimization with varying degrees of complexity. In Dienemann et al (2019) for example, the buckling of lightweight structures is considered for the optimization. But also such complex mechanical relationships as they occur in crash design can find consideration in topology optimization (e.g. Ortmann et al (2021)). Since the optimization often does not take the manufacturing process into account, the optimized structure still has to be post-processed. As a result, the mechanical structure sometimes loses its optimality significantly. For this reason, efforts have been made worldwide in recent years to take restrictions from special manufacturing processes into account in the optimization processes. The most considered manufacturing process is casting. A good overview of the processes and a comprehensive implementation can be found in Franke (2018). Numerous implementations can also be found on the relatively new manufacturing processes of additive manufacturing (e.g. Gaynor and Guest (2016)).

In this work, we focus on the integration of the most important manufacturing constraint of milling into the topology optimization with the level set method. This includes ensuring that complex shaped milling tools can reach any machining point of the structural surface, taking into account their tool holders, main spindle geometry and available machining directions.

This paper is organized as follows. First, previous research works are introduced in section 2. After that, level

Responsible editor: weihong zhang.

✉ Christopher Colling
christopher.colling@w-hs.de

[1] Chair for Optimization of Mechanical Structures, University of Wuppertal, Gaußstraße 20, 42119 Wuppertal, Germany

[2] Institute of Mechanical Engineering, Westfälische Hochschule Gelsenkirchen, University of Applied Sciences, Neidenburger Str. 43, 45897 Gelsenkirchen, Germany

set based topology optimization is briefly recapitulated in section 3. The newly developed method for considering the milling restriction is introduced in section 4. Then, the method is demonstrated with numerical examples in section 5. Finally, we finish this work with a Conclusion in section 6.

2 Related work

In application of the density method Guest and Zhu (2012), Chen et al (2016) and Vatanabe et al (2016) used projection methods to optimize manufacturable structures. The manufacturability is defined in such a way that the element densities can only increase or remain constant in the machining direction. If an element violates this constraint, it will be filled with structural material. While Guest and Zhu (2012) model a tool consisting of a cylinder and a hemisphere, no tool geometry is considered in the other mentioned works. Lee et al (2022) have recently extended the projection method for multi-axis machining. Langelaar (2019) developed a filter technique that can be used to optimize multi-axis millable structures. The core of the filter is the cumulative sum of the element densities in the machining direction. Multi-axis milling is achieved by rotating the element densities in the respective machining direction and afterward forming an intersection density field. The filter can take into account the geometries of the bit and holder. Mirzendehdel et al (2020) introduces an inaccessibility measure field. Thereby, manufacturability is integrated into the optimization problem as an explicit constraint.

Within the framework of the level set method, there are considerably fewer works to be found. Liu and Ma (2015) developed a method for optimizing 2.5D millable structures. This milling strategy is often used to manufacture components with surfaces aligned perpendicular to each other. The basic idea of the developed method is to influence the level set evolution in such a way that the optimized structures consist only of predefined and manufacturable basic geometric shapes. These can be cuboids, holes or simple freeform surfaces. Using the least squares method, the optimization is locally controlled to form the best-fitting shapes. Morris et al (2020) investigated a filtering technique for optimizing multi-axis millable structures using the level set method. The idea is to filter out the velocities that could lead to the creation of inaccessible areas by setting them to zero. At the same time, this prevents structural growth. The authors emphasize that this can lead to the emergence of weak local minimia. They modeled the milling tool by two hemispheres and two cylinders.

Deng et al (2022) developed a CAD-integrated approach of topology optimization considering millability. Their main idea is based on a projection method of structures composed of multiple CAD primitives to take into account multi-axis machining and possible subsequent application in CAD software. The geometry of the tool is not considered in the work.

Our approach is a follow-on from Morris et al (2020) work. Instead of using a technique to filter the level set evolution velocities and thus suppress structural growth, our approach is based on the sensitivities of an explicit milling constraint. Therefore, the direction of movement of the structural boundary is not immediately restricted. In combination with an augmented Lagrangian method, inaccessible boundaries are initially weakly stimulated to grow and more strongly as the optimization progresses. Furthermore, our approach can be used for realistic geometries of tool, tool holder and main spindle. Before we present our approach to considering millability we want to briefly summarize the level set based topology optimization approach.

3 Level set method based topology optimization

3.1 Definition of the optimization problem

The most famous optimization problem in the topology optimization of mechanical structures is the minimization of the mean compliance $C(\Omega)$ subjected to a volume constraint. According to Schumacher (2020), the mean compliance of a loaded structure is formally given by doubling the strain energy and can be mathematically described as

$$C(\Omega) = \int_\Omega \boldsymbol{f} \cdot \boldsymbol{u} d\Omega + \int_\Gamma \boldsymbol{g} \cdot \boldsymbol{u} d\Gamma = \int_\Omega \boldsymbol{\sigma}(\boldsymbol{u}) : \boldsymbol{\varepsilon}(\boldsymbol{u}) d\Omega \,, \quad (1)$$

where $\boldsymbol{f}$ stands for the body forces, $\boldsymbol{g}$ for the surface loads and $\boldsymbol{u}$ for the displacement field in the case of linear-elastic material behavior in the equilibrium state. The mean compliance can be expressed in terms of the stress tensor $\boldsymbol{\sigma}(\boldsymbol{u})$ and the strain tensor $\boldsymbol{\varepsilon}(\boldsymbol{u})$.

If the volume of the optimized structure should not exceed a certain value when minimizing the mean compliance, or, as in the present case, must reach a certain value V_z, the optimization problem can be defined as follows:

$$\begin{aligned} &\min C(\Omega) = \int_\Omega \boldsymbol{\sigma}(\boldsymbol{u}) : \boldsymbol{\varepsilon}(\boldsymbol{u}) d\Omega \\ &\text{subject to } V(\Omega) - V_z = \int_\Omega d\Omega - V_z = 0 \,. \end{aligned} \quad (2)$$

3.2 Shape representation by a level set function

The level set method developed by Osher and Sethian (1988) is an approach for numerical tracking of moving curves and surfaces. Within the context of topology optimization of

mechanical structures the n dimensional boundary Γ of a domain Ω is implicitly described by the zero level of a corresponding $n+1$ dimensional level set function. In several iterations, the level set function is developed in such a way that an objective function is minimized while fulfilling optimization constraints. The level set function $\varphi(\boldsymbol{x})$ is often defined as a signed distance function for which on every point $\boldsymbol{x} \in \mathbb{R}^n$ holds:

$$\varphi(\boldsymbol{x}) \begin{cases} > 0 \text{ if } \mathbf{x} \notin \Omega \\ = 0 \text{ if } \mathbf{x} \in \Gamma \\ < 0 \text{ if } \mathbf{x} \in \Omega\,. \end{cases} \tag{3}$$

By introducing a pseudotime $t \in \mathbb{R}^+$, the change in the structural boundary can be expressed as the motion of the boundary through a velocity field v_n normal to the boundary. The level set function can then be updated by solving the following Hamilton-Jacobi equation:

$$\frac{\partial \varphi}{\partial t} + v_n |\nabla \varphi| = 0\,. \tag{4}$$

Sethian (1999) shows suitable solution methods in the form of upwind schemes. For numerical reasons, the level set function can become very steep or very flat during evolution (van Dijk et al 2013). Since this negatively affects the evolution, the level set function is periodically reinitialized to the signed distance function. The still unknown velocity field is determined by a sensitivity analysis of the objective function and the optimization constraints.

3.3 Shape derivative

To determine a velocity field that minimizes a given functional, the concept of shape derivatives is used (Allaire et al 2004). If $\boldsymbol{\theta}(\boldsymbol{x}) \in \mathbb{R}^n$ is considered to be a sufficiently small displacement field, a transformation of a domain Ω into a perturbed domain Ω_t can be expressed as $\Omega_\theta = \{\boldsymbol{x} + t\boldsymbol{\theta} : \boldsymbol{x} \in \Omega\}$. Where the parameter t is used to scale the transformation. According to Sokolowski and Zolesio (1992) the shape derivative of a functional $J(\Omega)$ is defined as the following limit:

$$J'(\Omega)\boldsymbol{\theta} = \lim_{t \to 0} \frac{J\left(\Omega_t\right) - J(\Omega)}{t}. \tag{5}$$

Often the shape derivative takes the form

$$J'(\Omega)\boldsymbol{\theta} = \int_\Gamma \omega \boldsymbol{\theta} \cdot \boldsymbol{n} d\Gamma\,, \tag{6}$$

where $\omega \in \mathbb{R}$ is a scalar field and n is the outward-pointing normal unit vector field. In the case of minimization by the steepest descent method, according to Allaire et al (2004) the displacement field $\boldsymbol{\theta}$ can be chosen in such a way that a movement of the boundary in the normal direction causes a decrease in the functional. For this purpose, the displacement field $\boldsymbol{\theta} = -\omega \boldsymbol{n}$ is chosen. This results with equation 5 in

$$J\left(\Omega_t\right) = J(\Omega) - t \int_\Gamma \omega^2 d\Gamma + \mathcal{O}(t) < J(\Omega) \quad \text{with} \quad \lim_{t \to 0} \frac{\mathcal{O}(t)}{t} = 0\,, \tag{7}$$

where $\mathcal{O}(t)$ denotes the error in the linear approximation. As a velocity field for the level set equation, the normal component of the chosen displacement field $v_n = -\omega$ is used. If the introduced optimization problem is expressed, for example, in terms of a Lagrangian function to be minimized, this principle can be used to solve the presented optimization problem, as will be shown in the further course.

4 Topology optimization for milling suitable structures

We would now like to present our approach for considering manufacturability by milling processes. The approach is based on locating inaccessible structural regions and minimizing them through structural growth. Therefore, the accessibility constraint is specified first. Subsequently, a method for the detection of the inaccessible boundaries is presented using the example of 3-axis machining before finally a mathematical constraint is introduced.

4.1 Avoidance of inaccessible boundaries

4.1.1 Undercuts and tool collisions

Figure 1 shows how the accessibility of the structural surface for a milling tool can be restricted. The figure illustrates a mechanical structure that is to be manufactured from a blank using the sketched tool. Depending on the clamping of the workpiece on the machine table, different sides of the structure can be reached. In the following, this is taken into account by introducing machining directions. A 90° clockwise clamping of the workpiece is equivalent to machining from the drawn $+x$ machining direction. Consequently, machining can be performed from four different machining directions. (In the three-dimensional case, six machining directions are available.) In the example, three parts of the structural surface are inaccessible for the active machining direction.

The undercuts in areas (a) and (b) are inaccessible from all available machining directions, while area (c) could be reached by adding another machining direction ($-x$). Area b) shows that accessibility can be restricted not only by undercuts, but also by very deep and steep surfaces. This is due

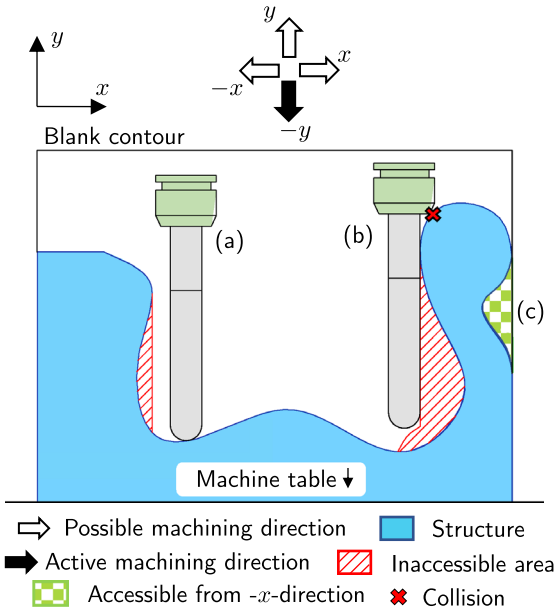

Fig. 1 Limitation of tool accessibility due to undercuts and deep surface areas

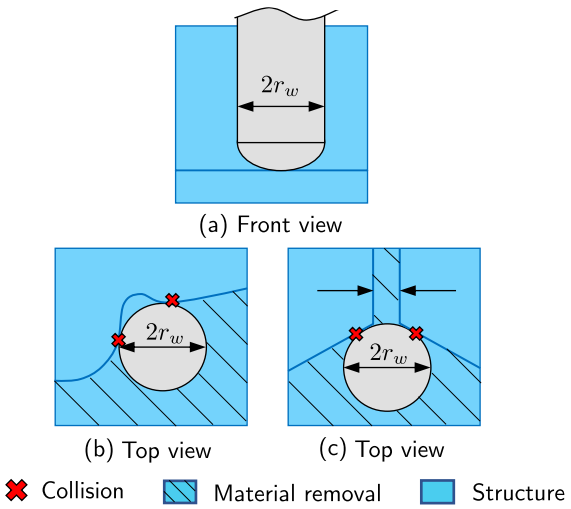

Fig. 2 Limitation of tool accessibility due to concave undercuts and thin cutouts

to the resulting collision between the tool holder and the structural surface.

4.1.2 Thin cutouts and concave curved surfaces

The accessibility of the structural surface can also be restricted by too large radii of the milling tool which is shown in Fig. 2. Figure 2a shows a milling tool with the radius r_w, which is used for the production of two example structures. In the two exemplary top views, the hatching indicates the areas where the material is to be removed. In Fig. 2b, it can be seen that inaccessible boundaries can be created by a local, high curvature of the structural surface. Choi (2001) also expresses these areas as concave undercuts. In addition, Fig. 2c shows that the minimum width of cutouts must be at least equal to the tool diameter $2r_w$.

4.2 Detection of inaccessible boundary points

This chapter introduces how to detect inaccessible boundaries. The detection of inaccessible boundaries is an important part of CAM software and is performed during the generation of toolpaths (Kief et al 2020). The basic procedure for the calculation of collision-free toolpaths is shown by Choi (2001).

Simplified methods can be used for exclusive collision detection. For example, Morris et al (2020) use a classical ray casting algorithm to detect inaccessible boundaries. In this work, an alternative method is introduced that is based on an interpolation of the level set function on the outer contours of the bit, tool holder, and main spindle. An advantage of this method is that the related geometries can be easily modified.

4.2.1 Tool accessibility

The following procedure is performed separately for each considered machining direction. Figure 3 serves as an introduction. A mechanical structure is shown which is to be manufactured from the machining directions $-y$ (left) and x (right). First, interpolation paths are defined, which extend from the boundary points of the structure along the negative machining direction to the boundary of the design space. If a negative value occurs at the interpolation point - i.e. the point lies in the structure (see equation 3) - the underlying boundary point is inaccessible for the current machining direction and is not further developed in the following (see interpolation path a)). If a boundary point is accessible no point on its associated interpolation path is determined as negative (see interpolation path b). The process is completed for the current machining direction when no more boundary points to be developed are left. If boundary points have been detected as inaccessible, the procedure is repeated for the next available machining direction, but only with the points that were inaccessible until then (see Fig. 3, right).

To integrate the tool geometry, the interpolation paths can now be modified. For example, the outer contour of a milling tool can be selected instead of a straight line. This is illustrated in Fig. 4 where a milling tool is shown together with its tool holder. Two interpolation paths are used to represent the complete outer contour, whereby four paths are used in

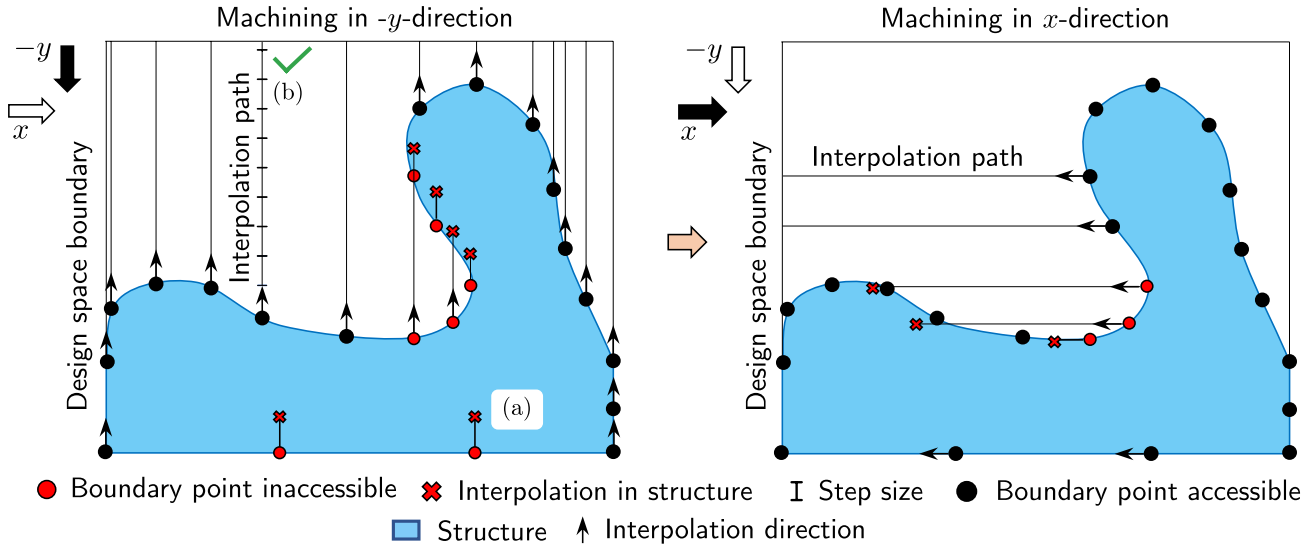

Fig. 3 Identification of inaccessible boundaries via interpolation of the level set function using the example of straight interpolation paths

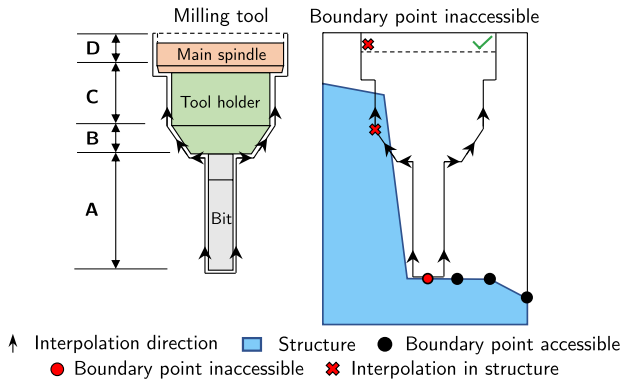

Fig. 4 Adaptation of the interpolation paths to the geometry of the bit, tool holder and main spindle (left). In the case of a collision (right), the boundary point is marked as inaccessible

the three dimensional case. In general, the four tool sections shown are subdivided as follows:

- *Section A*: Interpolation from the bottom of the bit to the bottom of the tool holder.
- *Section B*: Interpolation along the widening tool holder.
- *Section C*: Interpolation along the outer diameter of the tool holder.
- *Section D*: Interpolation along the outer casing of the main spindle and the permitted tool travel in axial direction.

For a boundary point to be marked as accessible, all interpolation paths in section A-D must reach the design space boundary without colliding. If one of the paths collides with the structure, the boundary point is marked as inaccessible (Fig. 4, right). In section D, the outer cladding of the axially movable main spindle can be modeled. Especially in the case of very bulky structures, collisions between the main spindle and the structure can occur. In practice, these collisions can often be avoided by using longer tool holders or milling tools. In addition, a maximum permissible traverse path of the main spindle in the machining direction can be specified in section D. This can be used, for example, to ensure that a residual material layer is maintained to the machine table. In this case, the interpolation path from the upper edge of the modeled main spindle to the design space boundary must not exceed the permissible traverse path. If the specified travel distance is exceeded, the corresponding boundary point is marked as inaccessible.

4.2.2 Definition of interpolation paths

This chapter shows how the previously introduced interpolation paths in sections A, B, C, and D are described mathematically. The interpolation paths are generally formulated for the three-dimensional case for any machining directions pointing in the direction of the coordinate axes. A machining direction is described in the further course as a unit vector $\boldsymbol{b}$ pointing in the respective direction. In order to assess the accessibility of a boundary point, the interpolation paths are evaluated along several interpolation points distributed along the corresponding path.

Section A

Figure 5 depicts how the interpolation paths in section A run. For this purpose, a bit is shown on the left side, which is used to machine a boundary point at the coordinates $\boldsymbol{x}_r$. Interpolation points are marked on the milling tool, which are traversed in n_A interpolation steps. The top right view shows

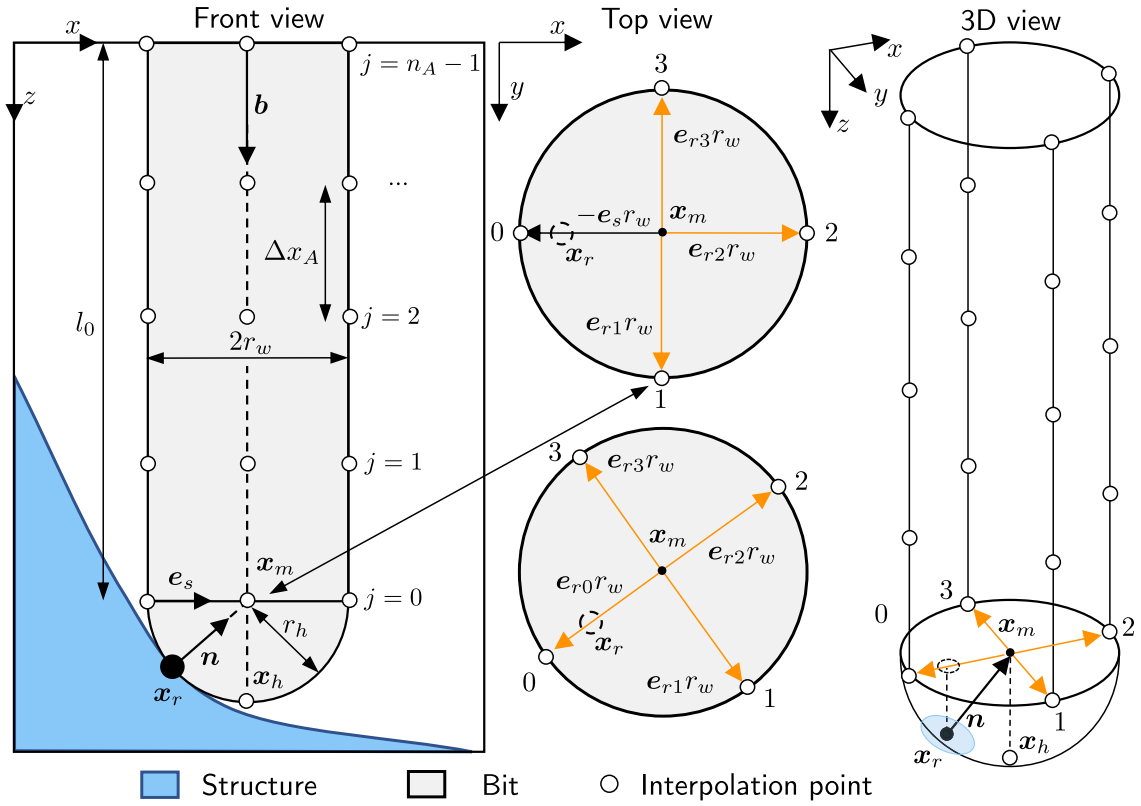

Fig. 5 Distribution of the interpolation points in section A

that the four interpolation paths are symmetrically distributed around the circumference. Each of the four paths has a starting point. The positions of the four starting points 0-3 depend on the orientation of the structural surface at the machining point. That orientation is captured by the normal unit vector $\boldsymbol{n}$. To calculate the starting points, the normal vector is mapped to the bottom of the cylindrical part of the milling tool. The resulting vector is then normalized to one. Formally, the described unit vector $\boldsymbol{e}_s$ can then be determined for a given machining direction as

$$\boldsymbol{e}_s = \frac{\boldsymbol{n} - \zeta(\boldsymbol{n}\cdot\boldsymbol{b})\boldsymbol{b}}{|\boldsymbol{n} - \zeta(\boldsymbol{n}\cdot\boldsymbol{b})\boldsymbol{b}|} \quad \text{with} \quad \zeta = 0.99\,. \tag{8}$$

In the above equation, the factor ζ is used to avoid a division by zero in case $\boldsymbol{n}\cdot\boldsymbol{b} = -1$ or $\boldsymbol{n}\cdot\boldsymbol{b} = 1$. With the help of this unit vector, four further unit vectors $\boldsymbol{e}_{ri}$, each offset by 90°, are defined. Each is aligned starting from the center of the bit in the direction of a respective interpolation starting point. For this purpose, the unit vector $\boldsymbol{e}_s$ is rotated around the current machining direction using a rotation matrix $\boldsymbol{R}_b$. On the bottom right top view in Fig. 5 the four resulting vectors can be seen. The chosen representation is valid for a generally oriented surface. Considering that $\boldsymbol{e}_{r0} = -\boldsymbol{e}_s$ on the one hand and $\boldsymbol{e}_{r2} = \boldsymbol{e}_s$ on the other hand, the coordinates of the four starting points can be calculated. At first the position of the bottom center point at coordinates $\boldsymbol{x}_m$ is calculated as

$$\boldsymbol{x}_m = \boldsymbol{x}_r + \boldsymbol{n}r_h\,. \tag{9}$$

Where r_h describes the radius of the tool head. Before the interpolation in section A takes place, the interpolation point at the head of the tool is evaluated. Its coordinates $\boldsymbol{x}_h$ are given by

$$\boldsymbol{x}_h = \boldsymbol{x}_m + \boldsymbol{b}r_h\,. \tag{10}$$

Starting from the center point, using the radius of the bit r_w, the starting points for the interpolation step $j = 0$ are as follows:

$$\begin{aligned}
\boldsymbol{x}_{A,0}^{j=0} &= \boldsymbol{x}_m - \boldsymbol{e}_s r_w &&= \boldsymbol{x}_m + \boldsymbol{e}_{r0} r_w \\
\boldsymbol{x}_{A,1}^{j=0} &= \boldsymbol{x}_m + \boldsymbol{R}_b\left(\frac{\pi}{2}\right)\boldsymbol{e}_s r_w &&= \boldsymbol{x}_m + \boldsymbol{e}_{r1} r_w \\
\boldsymbol{x}_{A,2}^{j=0} &= \boldsymbol{x}_m + \boldsymbol{e}_s r_w &&= \boldsymbol{x}_m + \boldsymbol{e}_{r2} r_w \\
\boldsymbol{x}_{A,3}^{j=0} &= \boldsymbol{x}_m - \boldsymbol{R}_b\left(\frac{\pi}{2}\right)\boldsymbol{e}_s r_w &&= \boldsymbol{x}_m + \boldsymbol{e}_{r3} r_w\,.
\end{aligned} \tag{11}$$

If the interpolation points are shifted in a total of n_A steps with $n_A \geq 2$ by the step size Δx_A in the negative machining

direction, the coordinates of the i interpolation paths to each interpolation step j can be calculated as

$$\boldsymbol{x}_{A,i}^{j} = \boldsymbol{x}_{A,i}^{j=0} - j\Delta x_A \boldsymbol{b} \quad \text{with} \quad j = 0, 1, ..., n_A - 1 \quad \text{and} \quad \Delta x_A = \frac{l_0}{n_A - 1}. \tag{12}$$

Where l_0 quantifies the distance from the bottom of the bit to the bottom of the tool holder.

Section B

The distribution of the interpolation points along the tool holder is shown in Fig. 6. After passing through section A, the last interpolated points are just at the level of the bottom side of the tool holder adjacent to the circumference of the bit. The starting points of the interpolation paths in section B are located on the bottom side of the tool holder with diameter d_1. Therefore, the four last interpolated points are offset in the directions $\boldsymbol{e}_{ri}$ by the amount a_1 (see Fig. 6, bottom). From this follows the starting points for section B as

$$\boldsymbol{x}_{B,i}^{j=0} = \boldsymbol{x}_{A,i}^{j=n_A-1} + \boldsymbol{e}_{ri} a_1 . \tag{13}$$

Subsequently, the interpolation is performed along the conical section of the tool holder. This has the height l_1. The radius of its cross-sectional area increases from the bottom to the top by the amount a_2. With a total of n_B steps with $n_B \geq 2$ and the step size Δx_B, the following then applies for the interpolation paths:

$$\boldsymbol{x}_{B,i}^{j} = \boldsymbol{x}_{B,i}^{j=0} + \frac{\left(\boldsymbol{e}_{ri} a_2 - \boldsymbol{b} l_1\right)}{\left|\boldsymbol{e}_{ri} a_2 - \boldsymbol{b} l_1\right|} j\Delta x_B \quad \text{with} \quad j = 0, 1, ..., n_B - 1 \quad \text{and} \quad \Delta x_B = \frac{\sqrt{a_2^2 + l_1^2}}{n_B - 1}. \tag{14}$$

Section C In section C, the interpolation path is defined using the same scheme as in section A (see Fig. 6). The starting points of the interpolation paths are the endpoints from the interpolation in section B

$$\boldsymbol{x}_{C,i}^{j=0} = \boldsymbol{x}_{B,i}^{j=n_B-1} . \tag{15}$$

The interpolation is performed in the direction of the negative machining direction over the length l_2 with a step size Δx_C. For a total of n_C steps with $n_C \geq 2$, the coordinates of the interpolation points result as

$$\boldsymbol{x}_{C,i}^{j} = \boldsymbol{x}_{C,i}^{j=0} - j\Delta x_C \boldsymbol{b} \quad \text{with} \quad j = 0, 1, ..., n_C - 1 \quad \text{and} \quad \Delta x_C = \frac{l_2}{n_C - 1}. \tag{16}$$

Section D

For the acquisition of the main spindle, the last calculated interpolation points from area C are offset in the directions $\boldsymbol{e}_{ri}$ by the amount a_3 (see Fig. 7). This results in the following interpolation starting points:

$$\boldsymbol{x}_{D,i}^{j=0} = \boldsymbol{x}_{C,i}^{j=n_C-1} + \boldsymbol{e}_{ri} a_3 . \tag{17}$$

The interpolation is performed along the outer contour of the main spindle over the height l_3. It is assumed that this can be moved axially over the distance s_v. For n_D steps with $n_D \geq 2$ and a step size Δx_D, the coordinates of the interpolation points then result in

$$\boldsymbol{x}_{D,i}^{j} = \boldsymbol{x}_{D,i}^{j=0} - j\Delta x_D \boldsymbol{b} \quad \text{with} \quad j = 0, 1, ..., n_D - 1 \quad \text{and} \quad \Delta x_D = \frac{l_3 + s_v}{n_D - 1}. \tag{18}$$

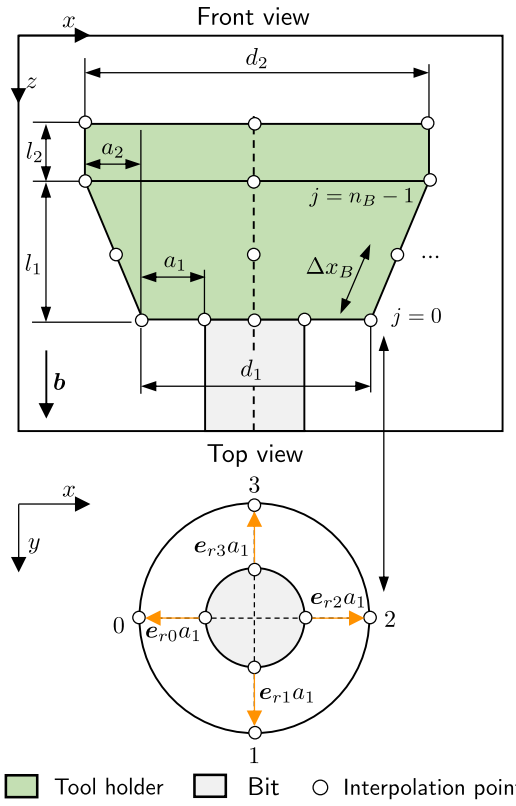

Fig. 6 Distribution of the interpolation points in sections B and C. Due to illustration reasons, the main spindle is not shown

4.3 Mathematical description of the manufacturing constraint

In the following, we will present the strategy used to integrate the previously presented manufacturing constraint into the topology optimization with the level set method. The goal of this strategy is to make all inaccessible surfaces

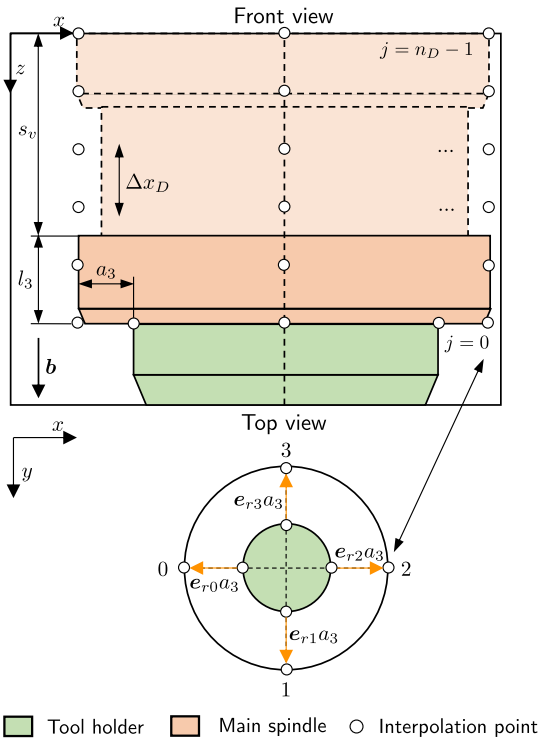

Fig. 7 Distribution of the interpolation points in section D

accessible during the optimization by inducing structural growth in this areas.

4.3.1 Transformation of the manufacturing constraint into a potential

For the derivation of an optimization strategy, please refer once again to Fig. 1. At positions (a) – (c), inaccessible areas are drawn as hatched areas. One way to remove the inaccessible areas is to fill them with structural material. However, it is also conceivable to remove the structural material above the inaccessible areas in order to make the areas below accessible. The latter variant, however, has the disadvantage that the structural areas to be removed cannot be identified using the interpolation method presented. Due to induced structural growth on the inaccessible surfaces, the structural volume increases. To comply with a volume restriction the structure needs to shrink in other areas. However, where this occurs depends on the sensitivities of the objective function and the given constraints. This effect provides targeted removal of structural mass consistent with the optimization. Therefore, in the further course, the approach is to fulfill the manufacturing constraint by inducing growth on the inaccessible structural boundary.

To stimulate structural growth on the inaccessible boundary, a potential is assigned to each point of the design space. The potential $p(\boldsymbol{x})$ acquires the following properties:

- At time $t = 0$, the structural boundary has the potential $\varepsilon \in \mathbb{R}$.
- The potential changes linearly on straight lines oriented normal to the structural boundary.
- Inside the structure, the potential values are greater than outside the structure.
- The potential is independent of the development of the level set function.

To define a potential with the above properties, the level set function is used, which is set in this work as a signed distance function. This already fulfills the second property mentioned above. If the level set function at a discrete time point $\varphi_0(\boldsymbol{x})$ is subtracted from the boundary value ε required above, the equation for the potential follows as

$$p(\boldsymbol{x}) = \varepsilon - \varphi_0(\boldsymbol{x}) \quad \text{with} \quad \varphi(\boldsymbol{x}, t = 0) = \varphi_0 \,. \tag{19}$$

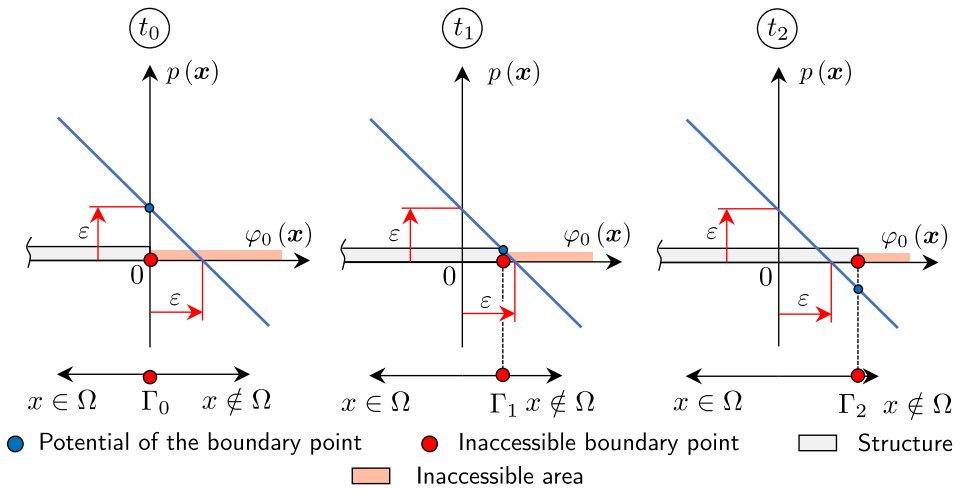

Fig. 8 Plot of the potential function of a one-dimensional structure at three different times $t_0 < t_1 < t_2$. The boundary point moves outwards

The goal now is to induce movement of the structural boundary by minimizing its boundary potential. Figure 8 illustrates this principle. The figure shows the time-constant potential function for a one-dimensional structure at three development steps. At the time t_0, the potential function is initialized, whereby the boundary potential assumes the value ε. To minimize the boundary potential, the boundary point shown must move to the right, i.e. to the outside. At the times t_1 and t_2 the potential thus has lower values than in the previous time steps. Note that if the potential function would be coupled with the evolution of the level set function, the boundary potential would always remain at ε. The potential on the structural boundary is now generally formulated as a boundary functional $U(\Omega)$

$$U(\Omega) = \int_\Gamma \eta p(\boldsymbol{x}) d\Gamma = \int_\Gamma \eta\big(\varepsilon - \varphi_0(\boldsymbol{x})\big) d\Gamma. \tag{20}$$

To separate inaccessible boundary regions Γ_S from the accessible regions, the factor η is introduced for which holds:

$$\eta = \begin{cases} 1 \text{ if } \Gamma \in \Gamma_S, \\ 0 \text{ if } \Gamma \notin \Gamma_S. \end{cases} \tag{21}$$

For $\varepsilon = 1$ the value of the functional just corresponds to the amount of the inaccessible structural surface. If all boundary points of the mechanical structure are accessible, the functional reduces to zero. Then the following condition must hold at a found optimum Ω_{opt}:

$$U\big(\Omega_{opt}\big) = \int_\Gamma \eta\big(\varepsilon - \varphi_0(\boldsymbol{x})\big) d\Gamma = 0. \tag{22}$$

4.3.2 Reinitialization of the potential function

If during an optimization, the inaccessible boundaries are moved outwards by a potential minimization, it must be determined again at regular intervals which parts of the structural boundary are inaccessible. Otherwise, already accessible structural boundaries could continue to be shifted by induced structural growth. This should be carried out in every iteration so that the factor η in equation 22 is as accurate as possible.

However, the potential function should also be regularly reinitialized. We have previously required that the potential is independent of the development of the level set function. As the optimization progresses, the current level set function differs more and more from the original one used to calculate the potential. If the topology changes during this time, the structural growth cannot be induced accurately at the respective locations. The principle of reinitialization is illustrated in Fig. 9. On the left side, the potential function $p^i(\boldsymbol{x})$ in iteration i is shown directly before its reinitialization. After the detection of inaccessible boundaries in the following iteration, the potential of the boundary points is raised again to the value ε. This is indicated on the right-hand side of the figure where the potential has been shifted upwards by a difference Δp. Reinitialization is done numerically by recalculating equation 19. Thereby, the level set function $\varphi_0^{i+1}(\boldsymbol{x})$ in iteration $i+1$ is used to obtain the potential $p^{i+1}(\boldsymbol{x})$. A suitable time to reinitialize the potential function is when the level set function is also reinitialized. The potential function can then directly obtain the properties of the signed distance function via the level set function.

4.4 Sensitivity analysis

To minimize equation 22, the sensitivities with respect to changes in the structural boundary need to be calculated. An advantage of the previously presented formulation of the manufacturing constraint is that by assuming a constant potential function, the calculation of the shape derivative is simplified. Using the shape derivative for boundary functionals (Allaire et al (2004), Lemma 5), the shape derivative of the boundary potential can be formulated as

$$U'(\Omega)\boldsymbol{\theta} = \int_\Gamma \left(\frac{\partial \eta p(\boldsymbol{x})}{\partial \boldsymbol{n}} + \kappa \eta p(\boldsymbol{x}) \right) \boldsymbol{\theta} \cdot \boldsymbol{n} d\Gamma + \int_\Gamma \eta p'(\boldsymbol{x}) d\Gamma. \tag{23}$$

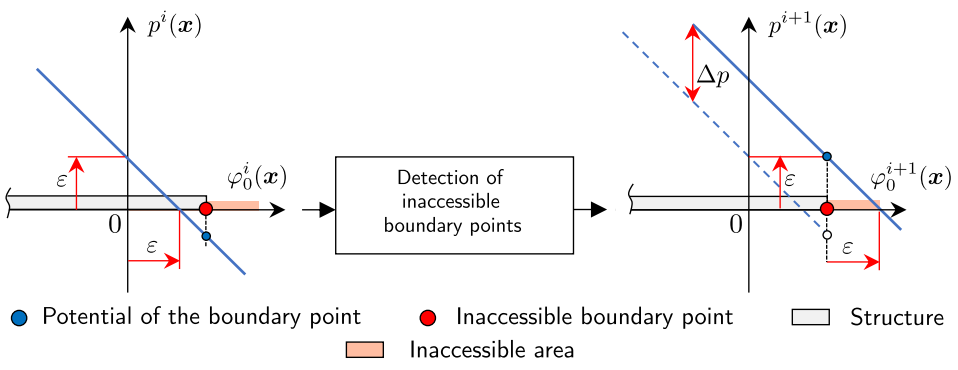

Fig. 9 Reinitialization of the potential function after a new detection of inaccessible boundary points between iteration i and iteration $i+1$

In this equation κ denotes the mean curvature. By defining the potential function via the signed distance function, the change of the potential in normal direction can be written as

$$\nabla p(\boldsymbol{x}) \cdot \boldsymbol{n} = -1. \tag{24}$$

The potential function is by definition independent of changes of the structural boundary. Therefore one can formally write

$$p'(\boldsymbol{x}) = 0. \tag{25}$$

Thus for the shape derivative of the boundary potential follows

$$U'(\Omega)\boldsymbol{\theta} = \int_\Gamma \eta\big(\kappa\big(\varepsilon - \varphi_0(\boldsymbol{x})\big) - 1\big)\boldsymbol{\theta} \cdot \boldsymbol{n} d\Gamma. \tag{26}$$

4.5 Augmented lagrangian and direction of steepest descent

To account for the manufacturing constraint during optimization, the classical optimization problem (equation 2) is first extended to include the introduced constraint:

$$\begin{aligned} \min J(\Omega) = C(\Omega) &= \int_\Omega \boldsymbol{\sigma}(\boldsymbol{u}) : \boldsymbol{\varepsilon}(\boldsymbol{u}) d\Omega \\ \text{subject to} \quad R_1(\Omega) &= \int_\Omega d\Omega - V_z = V(\Omega) - V_z = 0 \\ R_2(\Omega) &= \int_\Gamma \eta\big(\varepsilon - \varphi_0(\boldsymbol{x})\big) d\Gamma = 0. \end{aligned} \tag{27}$$

To solve the optimization problem, we use the augmented Lagrangian method in this work. For further information on this method, we refer here to Allaire et al (2016) and Nocedal and Wright (2006). In order to minimize an objective function $J(\Omega)$ with i equality constraints $R_i(\Omega)$, an augmented Lagrangian function $\mathcal{L}$ is formulated

$$\mathcal{L}(\Omega, \lambda, \Lambda) = J(\Omega) + \sum_{i=1}^{n} \lambda_i R_i(\Omega) + \sum_{i=1}^{n} \frac{1}{2\Lambda_i} R_i^2(\Omega). \tag{28}$$

Herein λ_i denote the Lagrange multipliers. The penalty parameters Λ_i are used to penalize violations of the restrictions. The penalty parameters are progressively reduced during the optimization, which corresponds to a strengthening of the penalty. The Lagrange multipliers and the penalty parameters are calculated per iteration k as follows:

$$\lambda_i^{k+1} = \lambda_i^k + \frac{1}{\Lambda_i^k} R_i(\Omega) \tag{29}$$

$$\Lambda_i^{k+1} = \alpha \Lambda_i^k. \tag{30}$$

The factor α is set in between $0 < \alpha < 1$. With the two considered restrictions, the augmented Lagrangian function to be minimized is formed according to equation 28 as

$$\begin{aligned} \mathcal{L}(\Omega, \lambda, \Lambda) = J(\Omega) &+ \lambda_1 R_1(\Omega) + \frac{1}{2\Lambda_1} R_1^2(\Omega) \\ &+ \lambda_2 R_2(\Omega) + \frac{1}{2\Lambda_2} R_2^2(\Omega). \end{aligned} \tag{31}$$

For an optimum Ω_{opt}, according to the Karush-Kuhn-Tucker conditions, the change of the Lagrangian function vanishes for a change of the structural boundary

$$\left.\frac{\partial \mathcal{L}}{\partial \Omega}\right|_{\Omega_{opt}} \boldsymbol{\theta} = 0. \tag{32}$$

If now the shape derivative of the Lagrangian function is formed, one obtains formally

$$\begin{aligned} \frac{\partial \mathcal{L}(\Omega, \lambda, \Lambda)}{\partial \Omega}\boldsymbol{\theta} = J'(\Omega)\boldsymbol{\theta} &+ \left[\lambda_1 + \frac{R_1(\Omega)}{\Lambda_1}\right] R_1{}'(\Omega) + \\ &\left[\lambda_2 + \frac{R_2(\Omega)}{\Lambda_2}\right] R_2{}'(\Omega). \end{aligned} \tag{33}$$

According to Allaire et al (2004), the shape derivative of the mean compliance (without considering body forces) as well as the shape derivative of the structural volume result in

$$J'(\Omega)\boldsymbol{\theta} = C'(\Omega)\boldsymbol{\theta} = -\int_\Gamma \boldsymbol{\sigma}(\boldsymbol{u}) : \boldsymbol{\varepsilon}(\boldsymbol{u})\boldsymbol{\theta} \cdot \boldsymbol{n} d\Gamma \tag{34}$$

and

$$R_1'(\Omega)\boldsymbol{\theta} = V'(\Omega)\boldsymbol{\theta} = \int_\Gamma \boldsymbol{\theta} \cdot \boldsymbol{n} d\Gamma. \tag{35}$$

With these two shape derivatives and the shape derivative of the boundary potential (equation 26) the derivative of the Lagrangian function can be written out as

$$\begin{aligned} \frac{\partial \mathcal{L}(\Omega, \lambda, \Lambda)}{\partial \Omega}\boldsymbol{\theta} = \int_\Gamma \Bigg(-\boldsymbol{\sigma}(\boldsymbol{u}) : \boldsymbol{\varepsilon}(\boldsymbol{u}) + \lambda_1 + \frac{1}{\Lambda_1}\left[\int_\Omega d\Omega - v_z\right] + \\ \left[\lambda_2 + \frac{1}{\Lambda_2}\int_\Gamma \eta d\Gamma\right]\eta\big(\kappa\big(\varepsilon - \varphi_0(\boldsymbol{x})\big) - 1\big)\Bigg)\boldsymbol{\theta} \cdot \boldsymbol{n} d\Gamma = \int_\Gamma \omega \boldsymbol{\theta} \cdot \boldsymbol{n} d\Gamma \end{aligned} \tag{36}$$

Finally, a velocity field for the level set evolution must be formed. As mentioned in the previous section in the case of minimization by the steepest descent method the displacement field $\boldsymbol{\theta}$ can be chosen in such a way that a movement of the boundary in the normal direction causes a decrease in the Lagrangian function. For this purpose, the displacement field $\boldsymbol{\theta} = -\omega \boldsymbol{n}$ is chosen. Now, to obtain an evolution velocity for the level set advection, one chooses the normal component

of the displacement field $v_n = \boldsymbol{\theta} \cdot \boldsymbol{n} = -\omega \boldsymbol{n} \cdot \boldsymbol{n} = -\omega$. After all, the velocity field is

$$v_n = \boldsymbol{\sigma}(\boldsymbol{u}) : \boldsymbol{\varepsilon}(\boldsymbol{u}) - \lambda_1 - \frac{1}{\Lambda_1}\left[\int_\Omega d\Omega - v_z\right] - \left[\lambda_2 + \frac{1}{\Lambda_2}\int_\Gamma \eta d\Gamma\right]\eta\big(\kappa\big(\varepsilon - \varphi_0(\boldsymbol{x})\big) - 1\big). \tag{37}$$

In equation 37, the part of the velocity belonging to the milling constraint is defined by the definition of η only on the structural boundary. However, since the level set equation is solved in the whole design space, we extrapolate the evolution velocity defined on the boundary with a normal velocity extension method proposed by Osher and Fedkiw (2003) into the design space.

4.6 Efforts to improve convergence behaviour

4.6.1 Memory field

The presented optimization procedure may lead to worse convergence behavior under the introduced velocity field (equation 37). This is because it can never be predicted whether the movement of the structural boundary will lead to new inaccessible boundary regions and where these regions will emerge. If an inaccessible region is moved outward while minimizing its boundary potential, this region will become accessible to the milling tool after a few iterations. This means that in this region the part of the velocity originating from the manufacturing restriction disappears. Now it can happen that via the remaining sensitivities of the objective function and constraints this area directly shrinks inwards and becomes inaccessible again. This leads to an oscillation of single structural regions around an accessible and inaccessible position over the iteration steps of the optimization.

To counteract this problem, a sensitivity field is introduced that is composed of sensitivities of the current iteration i and sensitivities of previous iterations $i-1$. Due to the information from previous iterations, growth is induced in the areas that have just become accessible and thus prevents a direct shrinking in the areas. The sensitivity field, called Memory Field in the further course, is calculated exclusively from the sensitivities of the manufacturing constraint. If the sensitivities from the shape derivative of the boundary potential are abbreviated as

$$U'(\Omega)\boldsymbol{\theta} = \int_\Gamma \frac{\delta U(\boldsymbol{x})}{\delta \Omega}\boldsymbol{\theta} \cdot \boldsymbol{n} d\Gamma \tag{38}$$

the Memory Field in iteration i can be defined as follows:

$$\left(\frac{\delta U(\boldsymbol{x})}{\delta \Omega}\right)^i_{Mem} = a\left(\frac{\delta U(\boldsymbol{x})}{\delta \Omega}\right)^i + (1-a)\left(\frac{\delta U(\boldsymbol{x})}{\delta \Omega}\right)^{i-1}_{Mem}. \tag{39}$$

The factor a with $0 < a \leq 1$ influences how strong the influence of past iterations is on the current iteration. The level set velocity field is then reformulated using the Memory Field as follows:

$$v_{n,Mem} = \boldsymbol{\sigma}(\boldsymbol{u}) : \boldsymbol{\varepsilon}(\boldsymbol{u}) - \lambda_1 - \frac{1}{\Lambda_1}\left[\int_\Omega d\Omega - v_z\right] - \left[\lambda_2 + \frac{1}{\Lambda_2}\int_\Gamma \eta d\Gamma\right]\big(\eta\big(\kappa\big(\varepsilon - \varphi_0(\boldsymbol{x})\big) - 1\big)\big)_{Mem}. \tag{40}$$

For the memory factor, we recommend to use a value of $0.5 \leq a \leq 0.8$. If the value is too low, the induced structural growth tends to become sluggish. This means that newly created inaccessible surfaces are only moved outwards with a significant delay. In addition, structural growth is maintained for a comparatively large number of iterations, even after accessibility has been achieved. This could lead to the formation of new, inaccessible surfaces in the vicinity of the last inaccessible surfaces that were moved outwards. This can result in the development of weak local minima and an increase in the number of iterations required. If the memory factor is set too high, the tendency of the above-described oscillations of the structural boundary around an accessible and inaccessible position increases.

4.6.2 Formation of sharp corners

Depending on the machining directions assumed for optimization, sharp edges and corners may have to be formed for full accessibility. This is illustrated in Fig. 10. If the percentage of inaccessible area falls below a threshold during optimization, we artificially help out with the formation of the corners. The threshold is chosen as 0.3% inaccessible surface. We interpolate the level set function in discrete steps on straight lines in the direction of the outward pointing normal unit vectors. We measure the distance $\Delta\varphi$ from each inaccessible node to the accessible area. Then we subtract this from the level set function values of the associated boundary nodes. We limit this boundary displacement by φ_{max} which is set to 0.3 times the element size.

5 Numerical experiments

Now the topology optimization under the influence of the presented manufacturing constraint is demonstrated by numerical examples. As such, we choose a loaded cube structure inspired by the SupportStruct example of Morris et al (2020), as well as a cantilever beam. In all numerical

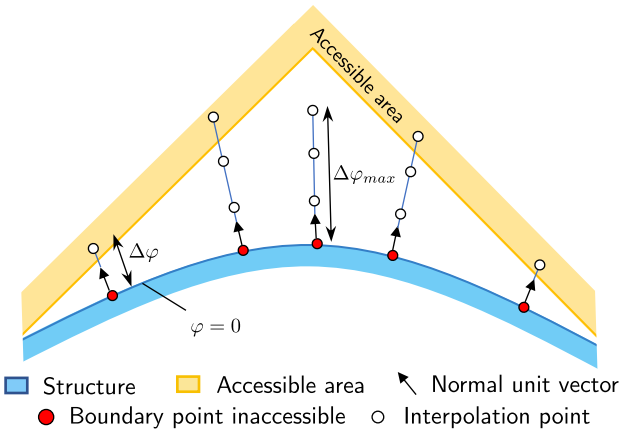

Fig. 10 Measurement of the distance from inaccessible boundary points to the accessible area in the normal direction. This distance is used to help out building sharp corners

experiments, optimization is first performed without taking into account the manufacturing constraint. Subsequently the influence of the manufacturing constraint on the optimization results is shown.

5.1 Implementation details

For discretization, the structural domain and design space are meshed by an unstructured finite element mesh. We resort to the work of Allaire et al (2013), where the structure is discretized by an adaptive mesh. In this process, the boundary nodes of the boundary elements are always positioned exactly at the zero level of the level set function during regular remeshing. The mesh of the structural domain can be extracted as a sub-mesh from the entire mesh consisting of the structural mesh and the mesh of the remaining, unfilled design space. Due to the fact that the boundary nodes always lie exactly on the zero level set, the boundary nodes are chosen as the boundary points introduced in the context of the interpolation procedure. The interpolation is realized numerically by a barycentric interpolation method. For this purpose, we use the open-source library 'Scipy'. For the solution of the level set advection equation, we resort to the positive coefficient scheme introduced by Sethian (1999). The finite element calculation is carried out on the solver 'OptiStruct' by Altair and is performed only on the structural mesh. After each finite element calculation, remeshing is performed along the zero level of the level set function. Thus, the level set function must be reinitialized in each iteration. As described before, after the level set reinitialization, a detection of inaccessible boundaries and a reinitialization of the potential function is performed.

The interpolation path step sizes should be set at least smaller than the element size in the case of structured grids. For an unstructured grid, as we have chosen, this should be at least one-third of the element size due to possible tapered geometry details. If the step sizes are too large, inaccessible boundaries are not reliably detected, which means that the optimized structure cannot be manufactured with the predefined tool. For this reason, an interpolation path step size of approx. 2.5 mm is selected in sections A-C and approx. 5 mm in section D. Due to the selected tool dimensions, section D is predominantly outside the design space. For efficiency reasons, the corresponding step size is doubled there.

We assume that the design space is the same as the blank used in manufacturing. Thus, all locations detected as inaccessible surfaces on the design space boundaries are considered as accessible. As a convergence criterion, we define that the constraints must be satisfied and, at the same time, the change in the objective function between two successive iterations must be less than 0.15%.

5.2 Optimization of a loaded cube structure

5.2.1 Optimization without manufacturing constraint

The cube shown in Fig. 11a with dimensions 300 x 300 x 300 mm is supported on four square faces ($\boldsymbol{u} = \boldsymbol{0}$). In the center of the top, the cube is loaded by a surface load ($g = 0.1\ \mathrm{N/mm^2}$) over a square area. The objective of the optimization is to minimize the mean compliance subjected to a volume constraint. The surface of the cube in Fig. 11a is selected as the boundary of the design space. Thereby, the volume of the structure should be reduced to 20% of the design space volume. As an initial design, the design space is completely filled with structural material whilst a spherical cutout with a diameter of 100 mm is placed in the center. The mean compliance is normalized in the following. If the entire design space is occupied by structural material, the cube structure has a normalized mean compliance of 1000. The Young's modulus is chosen as $E = 1\ \mathrm{N/mm^2}$ and the lateral contraction number as $\nu = 0.3$.

The optimization converges after 86 iterations. Thereby a normalized mean compliance of 1668 is obtained. In Fig. 11b the optimized structure is shown. Furthermore,

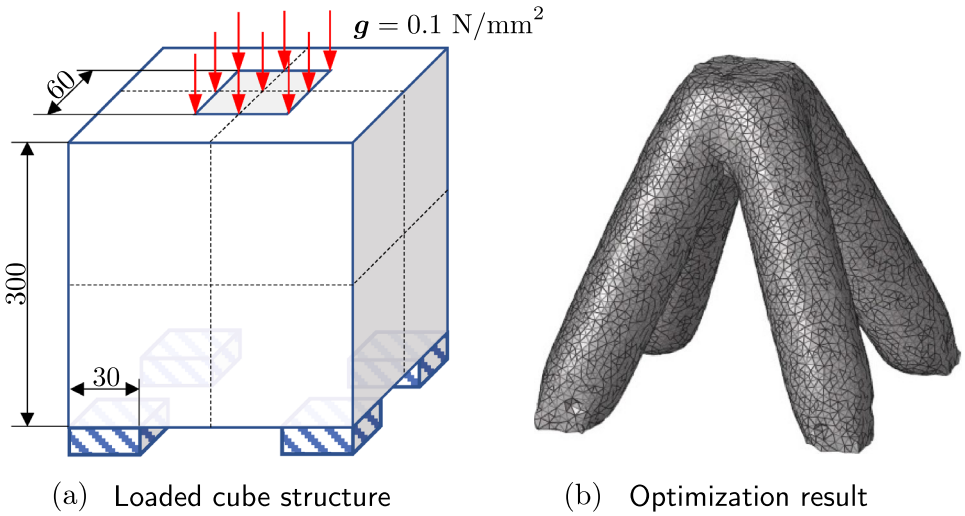

Fig. 11 Topology optimization of a loaded cube structure without considering the manufacturing constraint. All dimensions are given in mm

all numerical results are summarized in Table 1 in the first column.

5.2.2 Optimization with manufacturing constraint

We will now present the solution of the presented optimization task under the influence of the manufacturing constraint. For demonstration purposes, we perform the optimizations with two different milling tools. Tool a) has a bulky geometry while a more compact geometry is selected for tool b). The dimensions of the tools in comparison to the cube structure are shown in Fig. 12. Also, three different machining configurations are investigated for each tool. This means that machining is assumed from different directions and, at the same time, the number of machining directions is varied. In total, three different machining directions are investigated and are marked in Fig. 13. All previously mentioned material parameters are adopted for the following optimizations without modification. The introduced Memory Field is used as velocity field (see equation 40) with a memory factor $a = 0.65$. The optimization results for both tools under all investigated machining configurations are shown in Fig. 15. All optimized structures fulfill the specified volume constraint. Numerical results are listed in Table 1 for additional information.

The best overall optimization result of the series of experiments is obtained when using tool b) with machining configuration *II*. The associated optimization converges after 91 iterations. In the found optimum, a normalized mean compliance of 1799 is achieved. This value is 7.9% greater than that of the optimization without considering the manufacturing constraint.

As the worst result, the optimization considering tool a) using machining configuration *I* can be distinguished. The normalized mean compliance achieved is 3265 after a total

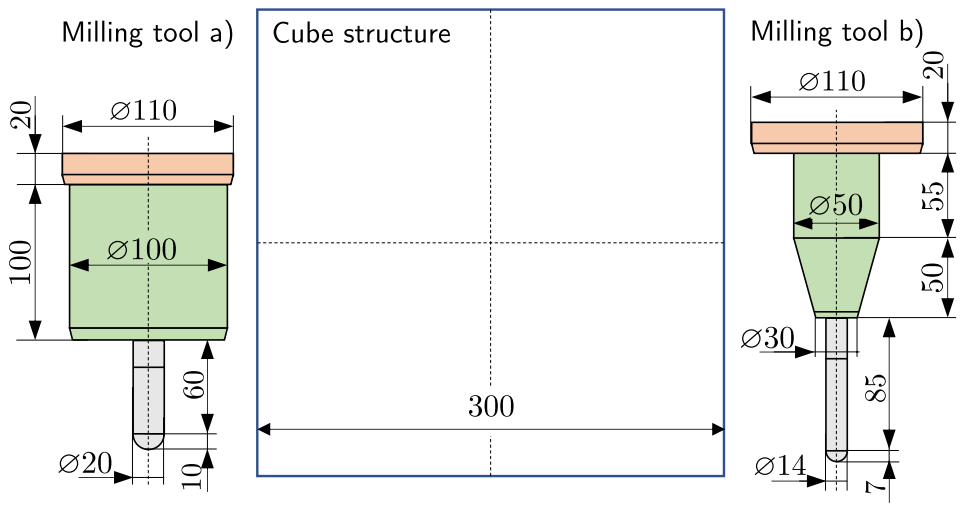

Fig. 12 Dimension of the two chosen milling tools(a) and (b) in comparison to the cube structure. All dimensions are given in mm

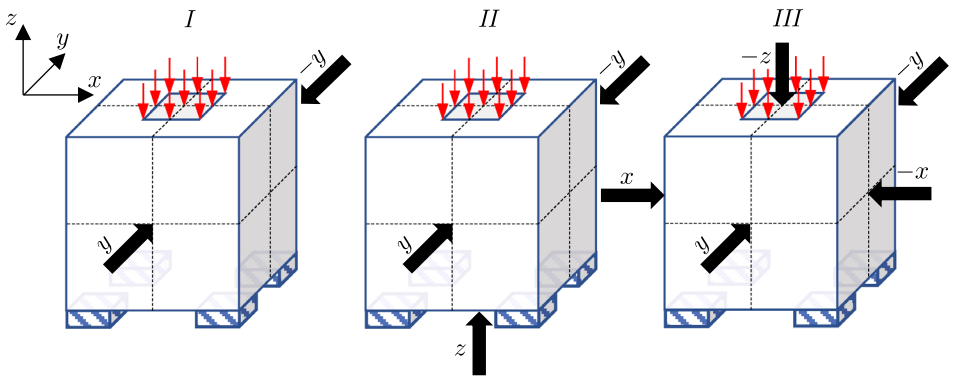

Fig. 13 Illustration of the three different machining configurations *I*, *II*, and *III*. The black arrows indicate the machining directions

of 110 iterations. In the found optimum, the value of the objective function is 95.7% percent greater than without considering the manufacturing constraint.

In Fig. 14 the convergence history of the inaccessible structural surface and the volume for the optimization with milling tool (a) under configuration *I* is shown as an example. It can be seen, that the minimization of the boundary potential continuously reduces the inaccessible surface. From iteration 30 to 65, the volume increases to meet the volume restriction. As a result, the amount of inaccessible surface temporarily stagnates at 16% before these are completely eliminated until the 68th iteration. Until the convergence criterion is met, the amount of inaccessible surface remains at almost 0%.

Although most machining directions are available in machining configuration *III*, this does not produce the best optimization results. The reason for this is that in Configuration *III* many surface portions are redundantly covered by the machining directions. In contrast, because of the available -z direction in configuration *II*, a structure can develope develop that resembles the structure that develops without taking the manufacturing constraint into account. The more the shape of the optimized structures under the influence of the manufacturing constraint resembles the structure without this constraint, the better are the optimization results. For this reason, better results are achieved with the more compact tool b) in all experiments. Its compact shape allows a more accurate mimic of this structure.

5.2.3 Impact of the memory factor

To demonstrate which impact the choice of the memory factor on the optimized structures has, we will now present the previous optimization task using tool a) under configuration *I* with two different memory factors. The first factor is set to $a_1 = 0.25$ and the second to $a_2 = 1$. Optimization results are shown in Fig. 16 and the numerical results are listed in Table 2.

As described above, a very low memory factor can lead to sluggish structural growth. This can be seen in the structure shown in Fig. 16 on the left. In this case, the low memory factor results in the inner arch of the structure not being able to regress. At the corresponding location (indicated by the red arrow), there is an increased amount of inaccessible boundaries during optimization, which leads to long-lasting

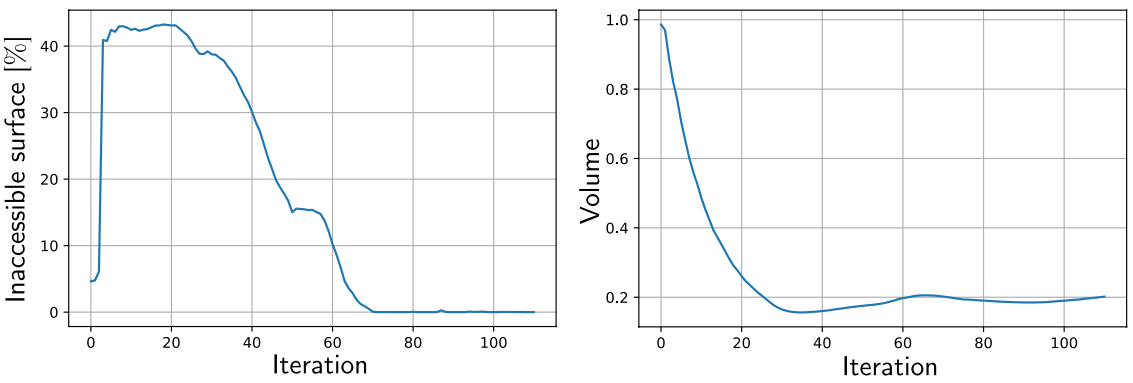

Fig. 14 Convergence history of the inaccessible structural surface and the volume during optimization with tool (a) under configuration *I*. The sudden increase in inaccessible surface in the first iterations is because the initial design is considered to be a blank and thus defined as fully accessible. The spherical cutout in the initial design is causing 5.0% of inaccessible surface in the initial design

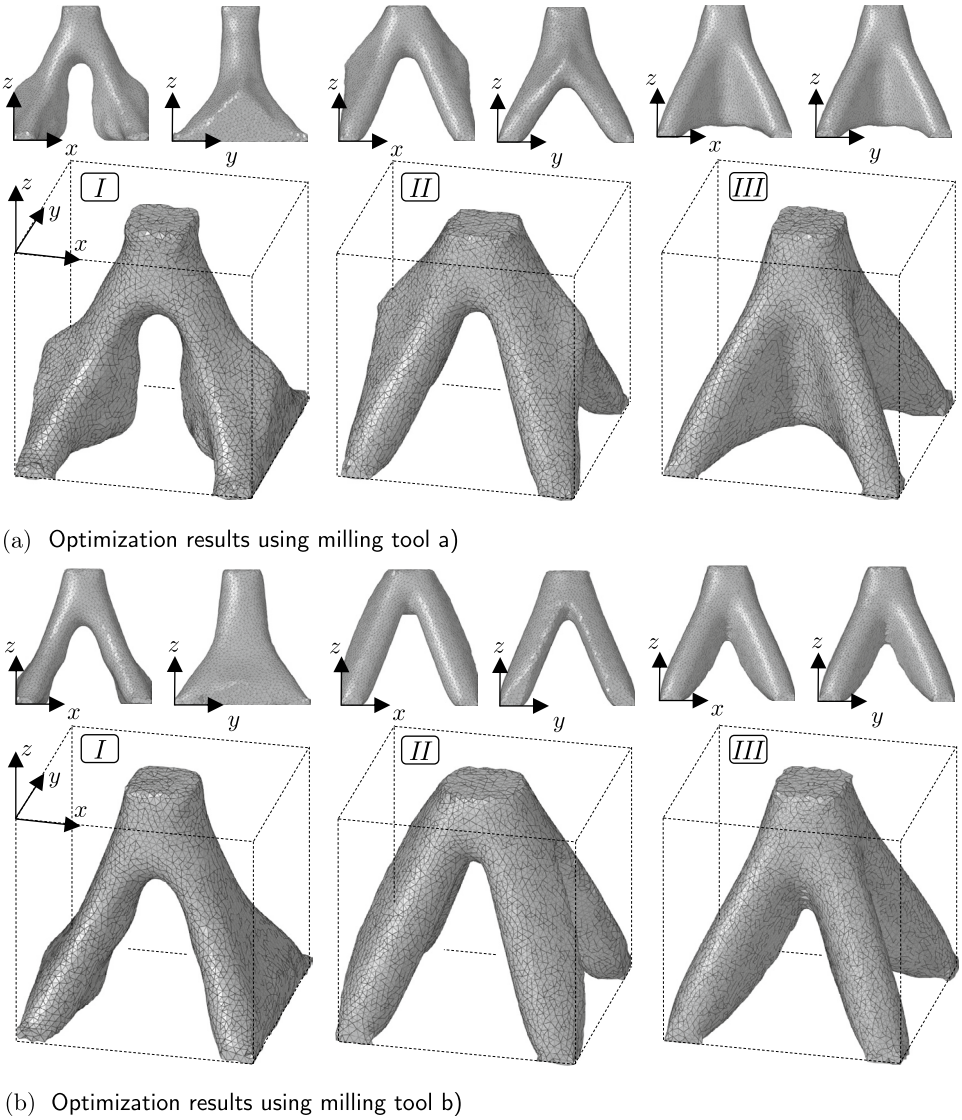

(a) Optimization results using milling tool a)

(b) Optimization results using milling tool b)

Fig. 15 Optimization results for the two chosen milling tools under every investigated machining configuration for the loaded cube structure

Table 1 Results of the performed optimizations of the loaded cube structure. The first column shows the results of the optimization without considering the manufacturing constraint. Information on percentage changes refers to this example

	–	Milling tool (a)			Milling tool (b)		
Machining configuration	–	I	II	III	I	II	III
Normalized mean compliance	1668	3265	1984	2190	2591	1799	1846
Increase in mean compliance (%)	–	95.7	18.9	31.2	55.3	7.9	10.7
Number of iterations	86	110	103	118	106	91	121
Increase in number of iterations (%)	–	27.9	19.8	37.2	23.3	5.8	40.7
Max. developed inaccessible surface	–	43.2	31.9	25.2	33.8	25.0	24.8

structural growth. Similarly, the normalized mean compliance has deteriorated to 3772, whereas here 151 iterations were necessary for convergence.

The optimization result for a high memory factor is shown on the right sight of figure 16. A memory factor of 1 means that no information from previous iterations is used to form the velocity field. With an achieved normalized mean compliance of 3272 this leads to almost the same mechanical properties as in the original example in the previous section 5.2.2, but the number of required iterations increases to 136 due to the onset of oscillations of the structural boundary around accessible and inaccessible positions.

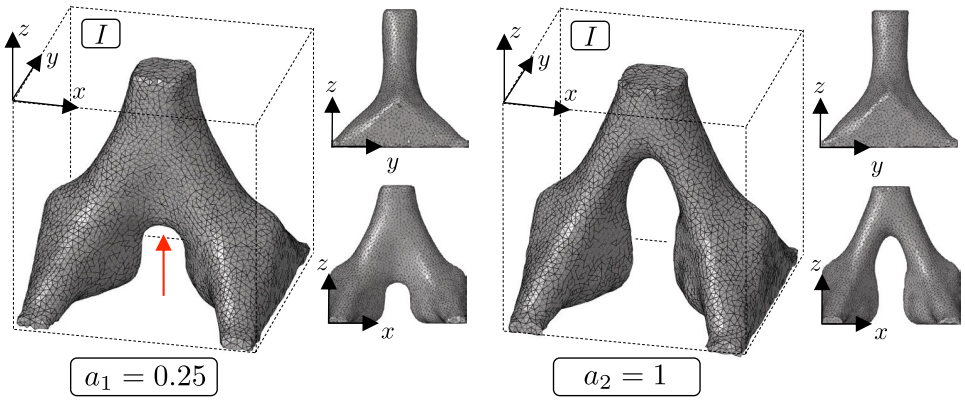

Fig. 16 Optimization results for the loaded cube structure using tool (a) under machining configuration *I* for two different memory factors *a*. The red arrow on the left structure indicates areas with long-lasting structural growth due to its low memory factor

Table 2 Optimization results of the loaded cube structure with different memory factors using tool a) under configuration *I*. The first column shows the results of the optimization without considering the manufacturing constraint. Information on percentage changes refers to this example

	–	Milling tool (a)		
Machining configuration	–	I	I	I
Memory factor	–	0.25	0.65	1
Normalized mean compliance	1668	3772	3265	3272
Increase in mean compliance (%)	–	126.1	95.7	96.2
Number of iterations	86	151	110	136
Increase in number of iterations (%)	–	75.6	27.9	58.1
Max. developed inaccessible surface	–	43.2	43.2	43.2

In practice, we recommend starting with the aforementioned high memory factor of 0.8. If the optimization converges very slowly, the memory factor should be reduced accordingly.

5.3 Optimization of a cantilever beam

5.3.1 Optimization without manufacturing constraint

As a further example, we will optimize the cantilever beam shown in Fig. 17a. The beam has dimensions of 900 x 300 x 300 mm and is supported on four square faces ($\boldsymbol{u} = \boldsymbol{0}$). The beam is loaded centrally on the front by a surface load

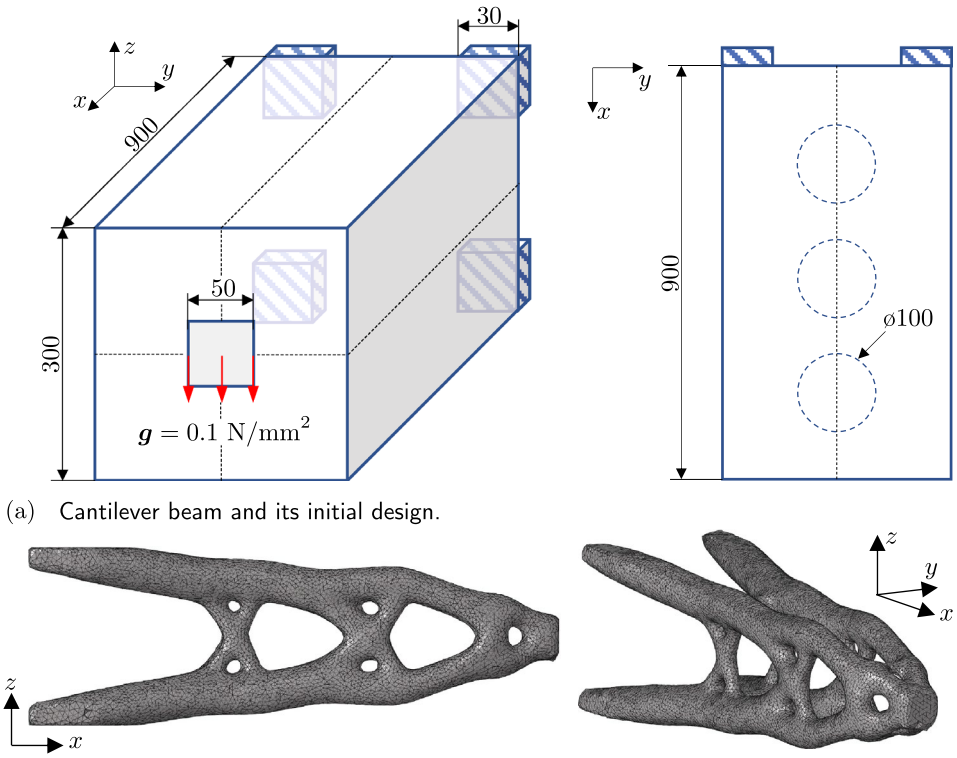

(a) Cantilever beam and its initial design.

(b) Optimization result

Fig. 17 Topology optimization of a cantilever beam. All dimensions are given in mm

($g = 0.1\,\mathrm{N/mm^2}$) over a square area. The objective of the optimization is to minimize the mean compliance subjected to a volume constraint. We chose the surface of the cantilever in Fig. 17a as the boundary of the design space. The volume of the structure should be reduced to 15% of the available design space volume. The mean compliance of the cantilever beam is normalized. As in the previous example, the structure has a normalized mean compliance of 1000 when the entire design space is filled with structural material. In the initial design, the design space is completely filled with structural material, whereby the 3 spherical cutouts with a diameter of 100 mm shown in Fig. 17a (right) are created along the longitudinal axis. These slightly increase the value of the objective function, so that the initial design has a normalized mean compliance of 1019. The Young's modulus is chosen as $E = 1\,\mathrm{N/mm^2}$ and the lateral contraction number as $\nu = 0.3$.

The corresponding optimization converges after a total of 68 iterations. Thereby, a normalized mean compliance of 3123 is achieved. Figure 17b shows the resulting structure. It can be seen that, in contrast to the previous example, numerous topology changes have taken place. Depending on the available machining directions and the existing tool geometry, these changes tend to increase the inaccessible surface.

5.3.2 Optimization with manufacturing constraint

In order to demonstrate the optimization taking into account the manufacturing constraints, two different tool geometries are once again defined. These are shown in Fig. 18. Two different machining configurations are assumed in this example, whereby the first configuration *I* consists of two and the second *II* consists of three machining directions. Both are shown in Fig. 19. All previously defined material parameters will be applied in the following. Again, the memory factor is set to $a = 0.65$. The structures resulting from the optimizations for both tools and machining configurations are illustrated in Fig. 20. All numerical results are presented in Table 3.

Altogether, the best result is obtained under configuration *II* with tool (d) after a total of 72 iterations. Its normalized mean compliance is 3183 and is thus 1.9% higher than without taking the manufacturing constraint into account. As the worst design the one under configuration *I* with tool (c) turns out. Here, after 78 iterations the achieved normalized mean compliance is 4886 and is thus 56.5% higher than without consideration of the manufacturing constraint.

Noticeable are the accumulations of structural material on the fixed rear side of the cantilever beam. Except for the experiment under configuration *II* with tool (d),

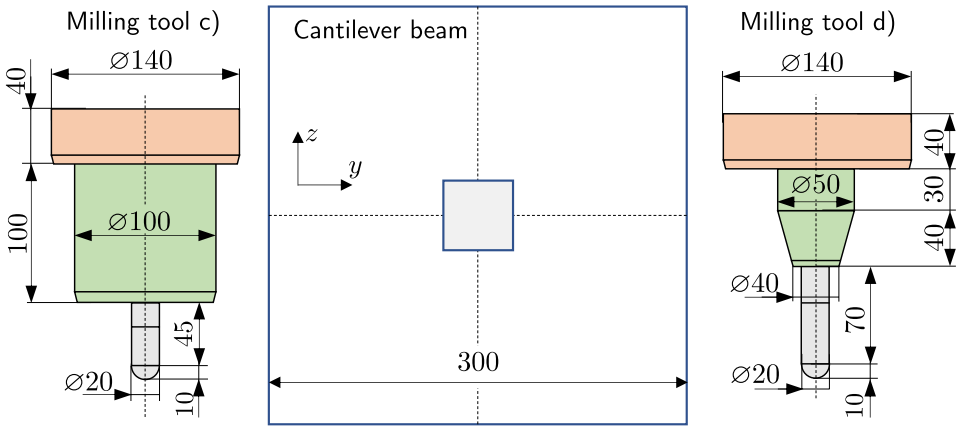

Fig. 18 Dimension of the two chosen milling tools (c) and (d) in comparison to the cantilever beam. All dimensions are given in mm

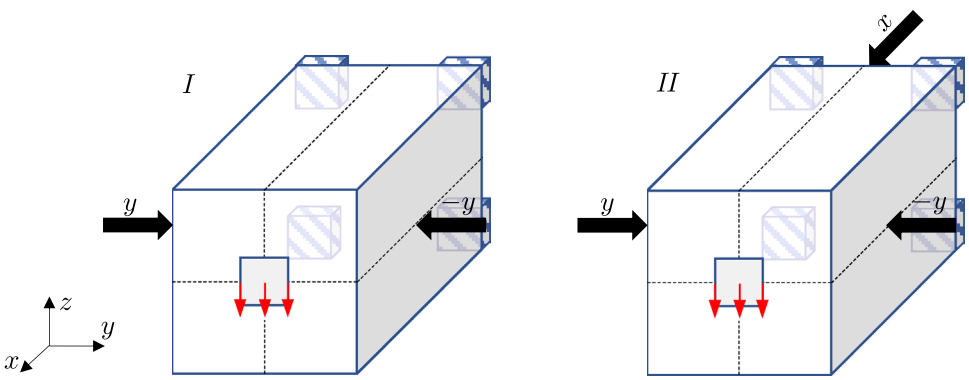

Fig. 19 Illustration of the two different machining configurations *I* and *II* for the cantilever beam. The black arrows indicate the machining directions

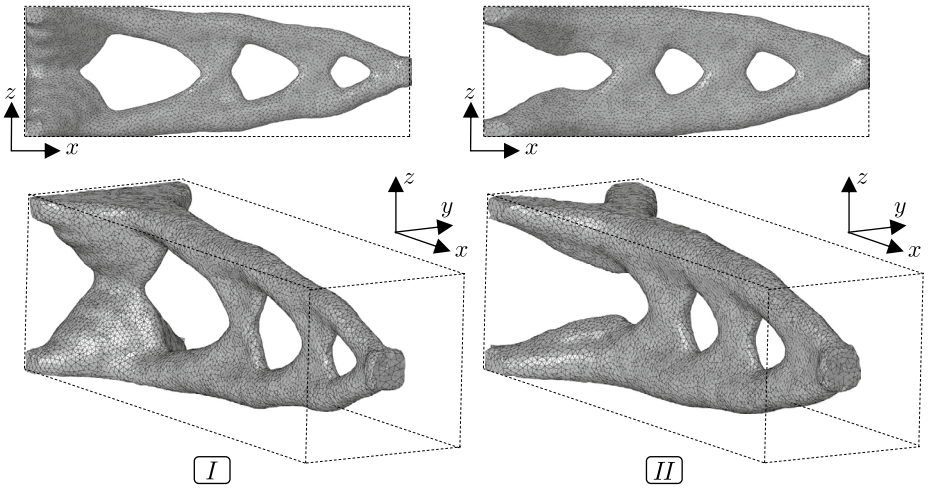

(a) Optimization results using milling tool c)

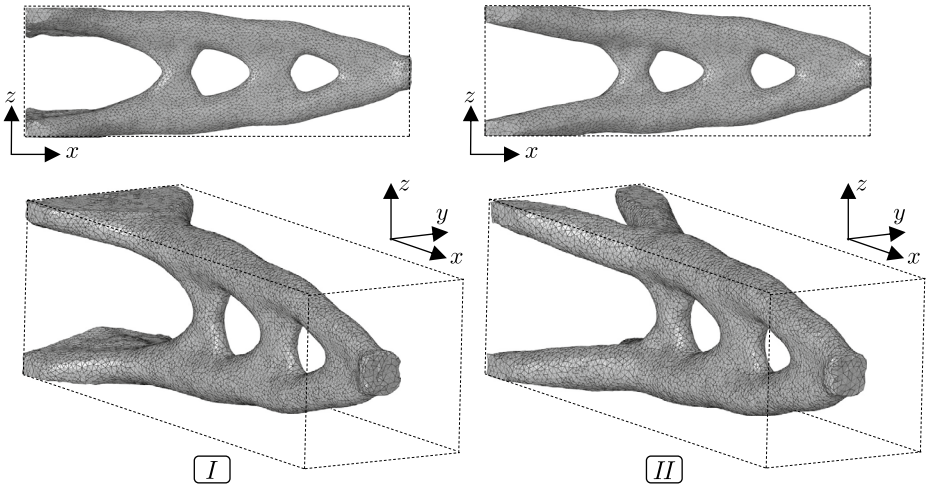

(b) Optimization results using milling tool d)

Fig. 20 Optimization results for the two chosen milling tools under both investigated machining configuration for the cantilever beam

Table 3 Results of the performed optimizations of the cantilever beam. The first column shows the results of the optimization without considering the manufacturing constraint. Information on percentage changes refers to this example

	–	Milling tool (c)		Milling tool (d)	
Machining configuration	–	I	II	I	II
Normalized mean compliance	3123	4886	3383	3965	3183
Increase in mean compliance (%)	–	56.5	8.3	27.0	1.9
Number of iterations	68	78	71	83	72
Increase in number of iterations (%)	–	14.7	4.4	22.1	5.9
Max. developed inaccessible surface	–	40.3	35.3	31.9	25.8

these accumulations always occur. In these areas, tool accessibility is limited. To fulfill the volume restriction, the structural material is shifted from mechanically more important locations to the described accumulations. This leads to the satisfaction of the volume constraint as well as the manufacturing constraint, but the compliance increases. With these experimental results, it is again underlined that the results strongly depend on the machining directions and the tool geometries. Also in this example the more compact tool d) leads to better results.

As an addition, the convergence histories for the inaccessible surface and the objective function for the experiment with tool (c) under configuration *I* are shown in Fig. 21 as an example. Due to the spherical cutouts in the initial design, the inaccessible surface in the first iteration equals 6.7%. From the 58th iteration on, the manufacturing constraint is fulfilled and is not violated in the subsequent optimization. In the next 20 iterations, the volume is slightly increased to meet the desired volume. Thereby, the mean compliance is minimized until the convergence criterion is fulfilled.

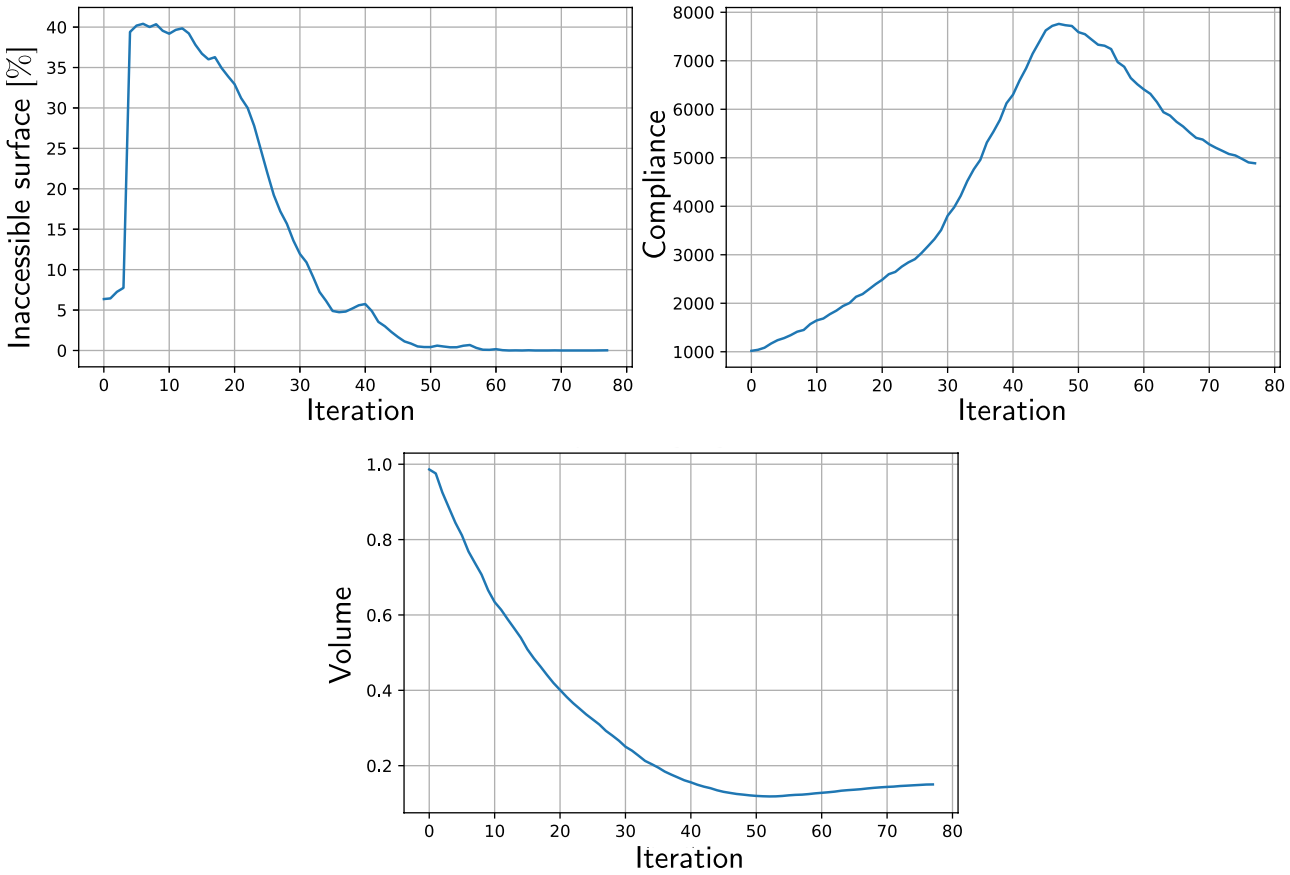

Fig. 21 Convergence history of the inaccessible structural surface, the normalized mean compliance and the volume for the experiment with tool (c) under configuration *I*. The spherical cutouts in the initial design are causing 6.7% of inaccessible surface in the initial design

In our implementation, we observed in all numerical experiments a percentage increase in iteration times of about 15% when using the manufacturing constraint compared to optimizations without this constraint.

6 Conclusions

In this paper, a method for topology optimization of millable structures using the level set method is developed using 3-axis milling as an example. A structure is classified as millable if, with predefined geometries of bit, tool holder, and main spindle as well as available machining directions, the entire structural surface is accessible to the milling tool. The presented interpolation method can be used for efficient detection of inaccessible boundaries and can be easily adapted to different tool geometries. By the definition of an outwardly decreasing and inwardly increasing potential field, controlled structural growth can be induced. The numerical examples show that minimizing the boundary potential leads to a minimization of the inaccessible surface. With the help of the Memory Field, which includes sensitivities averaged over several iterations, a good convergence behavior can be observed.

Nevertheless, the work is to be continued in the future. As a first step, we would like to extend the interpolation method to 5-axis machining. In addition, further investigations into potential clamping options for the workpieces are required. Furthermore, the optimization of the machining directions is to be investigated. Especially in the case of 3-axis machining, the number of machining directions allowed is a trade-off between manufacturing time and achievable mechanical properties. One strategy for finding the best machining directions could be to first perform the optimization without a manufacturing constraint and then select the machining directions based on the optimized structure. The machining directions should be selected in such a way that the largest possible area of the optimized structure is accessible. If in the example shown, manufacturing shall be done from two machining directions, the z-direction and the $-z$-direction will make the largest possible area of the structure accessible. This

strategy could also be automated during optimization. A prior optimization without manufacturing constraint is then not necessary. If the number of desired machining directions is specified, it is checked individually for all six possible machining directions which surface areas are inaccessible. Depending on the number of desired machining directions, those that can reach the largest total area, taking into account redundant ones, are then selected.

Finally, a comparison of existing methods for topology optimization considering millability is of interest as future work. For example, to clearly state that our approach has a reduced tendency to form weak local minima in the level set based approaches, further comparative experiments are necessary. Since several approaches also exist in the field of the density method, a comprehensive review of these and the approaches based on the level set method using a common benchmark problem could be beneficial, particularly with the inclusion of alternative objective functions.

7 Supplementary information

The convergence histories of the objective function as well as the used constraints of all performed numerical experiments can be downloaded as PDF files from the dataset Colling and Mecking (2023).

Funding Open Access funding enabled and organized by Projekt DEAL.

Declarations

Conflict of interest The authors declare that they have no Conflict of interest.

Replication of results The source code for generating the results shown is currently not publicly accessible. However, the authors believe that sufficient details of the demonstrated methodology have been described to reproduce the results. In case help is needed to reproduce the results or further implementation details are required, the corresponding author can be contacted.

References

Allaire G, Jouve F, Toader AM (2004) Structural optimization using sensitivity analysis and a level-set method. J Comput Phys 194(1):363–393. https://doi.org/10.1016/j.jcp.2003.09.032

Allaire G, Dapogny C, Frey P (2013) A mesh evolution algorithm based on the level set method for geometry and topology optimization. Struct Multidisc Optim 48(4):711–715. https://doi.org/10.1007/s00158-013-0929-2

Allaire G, Jouve F, Michailidis G (2016) Thickness control in structural optimization via a level set method. Struct Multidisc Optim 53(6):1349–1382. https://doi.org/10.1007/s00158-016-1453-y

Bendsøe MP, Sigmund O (2004) Topology Optimization, 2nd edn. Springer Berlin, Heidelberg,

Chen Y, Lu J, Wei Y (2016) Topology optimization for manufacturability based on the visibility map. Comput Aided Des Appl 13(1):86–94. https://doi.org/10.1080/16864360.2015.1059199

Choi BK (2001) C-space approach to tool-path generation for sculptured surface machining. In: Kimura F (ed) Geometric Modelling. Springer, US, Boston, MA, pp 85–97

Colling C, Mecking K (2023). Results of level set based topology optimizations considering the millability with realistic tools. https://doi.org/10.7910/DVN/ARCSD1,

Deng H, Vulimiri PS, To AC (2022) Cad-integrated topology optimization method with dynamic extrusion feature evolution for multi-axis machining. Comput Methods Appl Mech Eng 390:114456. https://doi.org/10.1016/j.cma.2021.114456

Dienemann R, Schumacher A, Fiebig S (2019) Considering linear buckling for 3d density based topology optimization. In: Rodrigues H, Herskovits J, Mota Soares C, et al (eds) EngOpt 2018 Proceedings of the 6th International Conference on Engineering Optimization. Springer, Cham, pp 394–406, https://doi.org/10.1007/978-3-319-97773-7_36

Franke T (2018) Fertigungsgerechte Bauteilgestaltung in der Topologieoptimierung auf Grundlage einer integrierten Gießsimulation. Logos Verlag Berlin GmbH

Gaynor AT, Guest JK (2016) Topology optimization considering overhang constraints: eliminating sacrificial support material in additive manufacturing through design. Struct Multidisc Optim 54(5):1157–1172. https://doi.org/10.1007/s00158-016-1551-x

Guest JK, Zhu M (2012) Casting and milling restrictions in topology optimization via projection-based algorithms. In: 38th Design Automation Conference, Parts A and B, pp 913–920, https://doi.org/10.1115/DETC2012-71507

Kief HB, Roschiwal HA, Schwarz K (2020) CNC-Handbuch - CNC, DNC, CAD, CAM, FFS, SPS, RPD, LAN, CNC-Maschinen, CNC-Roboter, Antriebe, Energieeffizienz, Werkzeuge, Industrie 40, Fertigungstechnik, Richtlinien, Normen, Simulation, Fachwortverzeichnis. Carl Hanser Verlag GmbH Co KG, https://doi.org/10.3139/9783446465244

Langelaar M (2019) Topology optimization for multi-axis machining. Comput Method Appl Mech Eng 351:226–252. https://doi.org/10.1016/j.cma.2019.03.037

Lee HY, Zhu M, Guest JK (2022) Topology optimization considering multi-axis machining constraints using projection methods. Comput Method Appl Mech Eng 390:114464. https://doi.org/10.1016/j.cma.2021.114464

Liu J, Ma YS (2015) 3d level-set topology optimization: a machining feature-based approach. Struct Multidisc Optim 52(3):563–582. https://doi.org/10.1007/s00158-015-1263-7

Mirzendehdel AM, Behandish M, Nelaturi S (2020) Topology optimization with accessibility constraint for multi-axis machining. Comput Aided Design 122:102825. https://doi.org/10.1016/j.cad.2020.102825

Morris N, Butscher A, Iorio F (2020) A subtractive manufacturing constraint for level set topology optimization. Struct Multidisc Optim. https://doi.org/10.1007/s00158-019-02436-y

Nocedal J, Wright SJ (2006) Numerical optimization, 2nd edn. Springer series in operations research, Springer, NY

Ortmann C, Sperber J, Schneider D et al (2021) Crashworthiness design of cross-sections with the graph and heuristic based topology optimization incorporating competing designs. Struct Multidisc Optim 64(3):1063–1077. https://doi.org/10.1007/s00158-021-02927-x

Osher S, Fedkiw R (2003) Level set methods and dynamic implicit surfaces, 1st edn. 153, Springer New York, NY, https://doi.org/10.1007/b98879

Osher S, Sethian JA (1988) Fronts propagating with curvature-dependent speed: algorithms based on hamilton-jacobi formulations. J Comput Phys 79(1):12–49. https://doi.org/10.1016/0021-9991(88)90002-2

Schumacher A (2020) Optimierung mechanischer Strukturen: Grundlagen und industrielle Anwendungen, 3rd edn. Springer Vieweg Berlin, Heidelberg

Sethian JA (1999) Level set methods and fast marching methods: evolving interfaces in computational geometry, fluid mechanics, computer vision, and materials science, 2nd edn. 3, Cambridge University Press

Sokolowski J, Zolesio JP (1992) Introduction to Shape Optimization - Shape Sensitivity Analysis, 1st edn. Springer Berlin, Heidelberg

van Dijk NP, Maute K, Langelaar M et al (2013) Level-set methods for structural topology optimization: a review. Struct Multidisc Optimn 48(3):437–472. https://doi.org/10.1007/s00158-013-0912-y

Vatanabe SL, Lippi TN, Lima CRd et al (2016) Topology optimization with manufacturing constraints: A unified projection-based approach. Advances in Engineering Software 100:97–112. https://doi.org/10.1016/j.advengsoft.2016.07.002